Chinese Journal of Aeronautics, (2020), 33(9): 2313–2328

Chinese Society of Aeronautics and Astronautics
& Beihang University

Chinese Journal of Aeronautics

cja@buaa.edu.cn
www.sciencedirect.com

CFD simulation of helicopter rotor flow based on unsteady actuator disk model

G.N. BARAKOS [a], T. FITZGIBBON [a], A.N. KUSYUMOV [b,*], S.A. KUSYUMOV [b], S.A. MIKHAILOV [b]

[a] *James Watt School of Engineering, Glasgow University, Glasgow G12 8QQ, United Kingdom*
[b] *Department of Aerohydrodynamics, Kazan National Research Technical University named after A.N.Tupolev, Kazan 420111, Russia*

Received 19 September 2019; revised 26 November 2019; accepted 18 February 2020
Available online 18 June 2020

KEYWORDS

CFD;
Fully resolved blades rotor;
PSP rotor;
Surface circulation distribution;
Unsteady actuator disk model

Abstract Actuator Disks (AD) can provide characterizations of rotor wakes while reducing computational expense associated with modeling the fully resolved blades. This work presents an unsteady actuator disk method based on surface circulation distribution combined with empirical data, blade element theory and rotor momentum theory. The nonuniform circulation distribution accounts for 3D blade load effects, and in particular, tip loses. Numerical simulations were conducted for the isolated pressure sensitive paint model rotor blade in hover and forward flight using the HMB3 CFD solver of Glasgow University. Validation of CFD results in comparison with published numerical data was performed in hover, for a range of blade pitch angles using fully turbulent flow and the k-ω SST model. In forward flight, the vortex structures predicted using the unsteady actuator disk model showed configurations similar to the ones obtained using fully resolved rotor blades. Despite the reduced grid cells number, the CFD results for AD models captured well the main vortical structures around the rotor disk in comparison to the fully resolved cases.

1. Introduction

CFD analyses for rotary wings with fully-resolved rotor blades are still expensive and may not be necessary for certain studies, like investigations of far-wakes of rotors, or rotor wake interactions and wake encounters. In Ref. 1, it is noted, that despite of significant progress CFD methods for fully resolved blades simulation in wind turbine aerodynamics simple, inexpensive methods are still actual in design and aeroelasticity applications. For example, Blade Element Momentum (BEM) theory methods provide comprehensive tool for wind turbines, but only under the simplest conditions: constant wind speed with zero yaw error.[2]

More advanced approach occupying a fidelity space between CFD methods for fully resolved blades simulation and comprehensive methods are source-based methods, including actuator lines and actuator disks, can provide characterizations of rotor wakes while reducing computational expense associated with modeling the fully resolved blades.

For this reason, actuator models of rotors and propellers have their place in the tool-chain of engineering

* Corresponding author.
E-mail address: postbox7@mail.ru (A.N. KUSYUMOV).

https://doi.org/10.1016/j.cja.2020.03.021

Nomenclature

a	free stream speed of sound
a_∞	lift curve slope
F	rotor disk area
C_p	pressure coefficient
C_T	rotor thrust coefficient
c	blade section chord
M_x	rolling moment
M_z	pitching moment
Ma_{tip}	blade-tip Mach number
$C_n Ma_{\text{tip}}^2$	normal force coefficient
N	number of rotor blades
Δp	disk loading (jump across the rotor disk surface)
Δp_{a}	average pressure disk loading
r	blade radial position
R	rotor radius
T	rotor thrust
x, y, z	axes of Cartesian coordinate system
x_1, y_1, z_1	axes of skewed coordinate system
U	tangential component of resultant rotor velocity
V	forward rotor velocity
V_{tip}	the blade tip speed
α	incidence angle
α_r	rotor disk plane tilt angle, with respect to the flight path
Γ	rotor circulation
Γ_{B}	circulation corresponding to a single blade
Γ_0	average circulation distribution
γ	circulation per length
δ	angle of vortex cylinder slope
θ	blade pitch angle
ϕ	angle of resultant velocity at blade to reference plane
μ	rotor advance ratio
λ	non-dimensional induced velocity
ρ	density of air
σ	rotor solidity
ψ	azimuth angle
Ω	blade rotational speed, radians per second
AD	Actuator Disk
CFD	Computational Fluid Dynamics
HMB	Helicopter Multi Block CFD solver
BET	Blade Element Theory
RMT	Rotor Momentum Theory
VBA	Virtual Blades Actuator
PSP	Pressure Sensitive Paint

methods available to helicopter designers. An advantage of the Actuator Disk (AD) models is easy implementation on any computational mesh and low demand for computer recourses.

Actuator-lines method[3] is a variant of the actuator-blade method whereby the blades are modeled by forces acting along filaments sources lines. These body forces are typically derived from a BEM method using tabulated airfoil data. To avoid discontinuities, each line's loading is distributed over grid points using a "regularization function" that spreads a sources influence at a distance away. Churchfield et al.[4] presents recent advances in the actuator-lines method and improved, higher fidelity, actuator-line implementation.

Classic actuator disk models allow the use of steady-state CFD, significantly reducing the required computer time and memory. The actuator disk approximates the rotor using an infinitely thin source of momentum modeled as a pressure jump across the disk. Between fully resolved blades with detailed CFD grids around them, and blade element momentum models of rotors, actuator disks can reproduce rotor/body interaction or rotor installation effects.

The momentum source is not affected by the presence of other rotors or a fuselage. For this reason, the effect of the rotor disk is simplified and the method, although computationally efficient, can only be used for initial estimates of the fuselage loads[5–7] or wake interactions with certain parts of the fuselage. The other restriction of this formulation is that is valid only for trimmed conditions and only allows for time averaged estimates of rotor-body interactions.

If needed, an AD can be converted to actuator line method, and can be used to provide some wake structure in the rotor near-field, as well as periodic, instead of averaged forcing on other rotors or on fuselage parts.

In reality, the effect of blades on the fuselage is unsteady. For this reason, the vortical structure of the flow around a fuselage in rotor-body interaction is different than what is predicted by steady-state actuator-disk methods. This problem can be partly solved using unsteady actuator disk models,[8] popular for flows around propellers. The disk surface is divided in the azimuthal direction, while a time-varied pressure jump and a tangential velocity are specified.[2,9] The flow parameters are updated with respect to the azimuth angle at each time step to simulate the unsteady flow effect induced by the rotating blades. Unlike actuator line methods, the AD approach does not require averaging of the source data to prevent singularities. The unsteady AD approach was used in Refs. 9,10 for simulation of rotor/fuselage interactions. In Ref. 11 the AD method was established in order to calculate the unsteady aerodynamic characteristics of a tilt-rotor in a conversion mode.

For current time accurate implementation of the AD method is a state of art problem requiring description of forces distribution acting on the disc actuator surface. This requires to determine the intensity of the AD sources intensity and then to add the corresponding body forces to the Navier-Stokes equations. Since no surface is needed in the grid, the position of the sources can be changed without transformation of the initial grid.

In addition, appropriate theory must be used to determine the AD source intensity. In most published references the body forces are typically derived from a BEM method that uses tabulated airfoil data.[2,9,12] This classic BEM method is based on strip theory and requires corrections particularly near the blade tip region, where tip loss effects are present. In Ref. 2, it is noted that such correction can be applied using Prandtl's approach.[13]

This paper adopts a different approach using AD to approximate the wake structure of a rotor in hover or forward flight. The AD implementation is similar to Lynch et al.[2] and is based on momentum sources. The advantage of this approach is that it does not require significant rearrangement of the CFD girds used for example for isolated fuselage computations.

Most AD methods apply time-varied sources distributed on the disc actuator surface in the form of a pressure jump. The pressure jump can be localized at an "active" part of the actuator disk where the blades are present. The extend of this "active" part corresponds to the planform of a fully resolved blade. In Refs. 10,11, such approach was termed unsteady Virtual Blades Actuator (VBA) model.

For structured hexa-grids the implementation of the AD disk models both special types of boundary conditions, and embedding of body force terms in the Navier–Stokes equations can be used. Using local grid refinement for structured hexa-grid allows for efficient and accurate identification of the disk area covered by the rotor blades, followed by the addition of a momentum source.[2]

Although several AD models are available in the literature, some nonuniform models have not been presented in any detail before, and are given here as an alternative to existing AD models. In this paper the pressure jump across the AD induced by the blades is estimated using prescribed circulation distributions. The nonuniform circulation distribution accounts for 3D blade load effects, and in particular, tip loses.

The AD model is used here for simulations of rotor flow wakes employing the Pressure Sensitive Paint (PSP) rotor[14] and results are compared with computations with fully resolved rotor blades. Results of the vortex structure visualization show the rotor wake configuration similar to the fully resolved rotor blades simulation in forward flight.

2. CFD flow solver and aerodynamic models

All calculations were performed using the parallel CFD solver HMB3[14] (Helicopter Multi Block) solves the dimensionless 3D Navier-Stokes equations in integral form using the Arbitrary Lagrangian Eulerian (ALE) formulation for time-dependent domains with moving boundaries:

$$S = \frac{\mathrm{d}}{\mathrm{d}t}\int_{V(t)} \boldsymbol{W}\mathrm{d}V + \int_{\partial V(t)} (\boldsymbol{F}_{\mathrm{i}}(\boldsymbol{W}) - \boldsymbol{F}_{\mathrm{v}}(\boldsymbol{W}))\cdot \boldsymbol{n}\mathrm{d}S$$

where $V(t)$ is the time dependent control volume, $\partial V(t)$ its boundary, $\boldsymbol{W}$ is the vector of the conservative variables $[\rho, \rho u, \rho v, \rho w, \rho E]^{\mathrm{T}}$, and $\boldsymbol{F}_{\mathrm{i}}$ and $\boldsymbol{F}_{\mathrm{v}}$ are the inviscid and viscous fluxes.

The viscous stress tensor is approximated in HMB3 using the Boussinesq hypothesis,[15] complemented by different turbulence models including one equation models of the Spalart-Allmaras family[16,17] and two-equation models of k-ω family.[18–20] Algebraic Reynolds stress models are also available.

The Navier-Stokes equations are discretised on the multi-block grid, using a cell-centered finite volume approach. A curvilinear coordinate system is adopted to simplify the formulation of the discretized terms, since body-conforming grids are adopted. The system of equations to be solved is:

$$\frac{\mathrm{d}}{\mathrm{d}t}\left(\boldsymbol{W}_{i,j,k}v_{i,j,k}\right) + \boldsymbol{R}_{i,j,k} = 0$$

where $\boldsymbol{W}_{i,j,k}$ is the vector of conserved variables in each cell, $v_{i,j,k}$ denotes its volume and $\boldsymbol{R}_{i,j,k}$ represents the flux residual.

The upwind scheme proposed by Osher and Chakravarthy[21] is used to resolve the convective fluxes for its robustness, accuracy and stability properties. The Monotone Upstream-centered Schemes for Conservation Laws (MUSCL) variable extrapolation method[22] is employed in conjunction to formally provide second-order accuracy. Van Albada et al.[23] is also applied to remove any spurious oscillations across shock waves. The integration in time is performed with an implicit dual-time method to achieve fast convergence. The linear system is solved using a Krylov subspace algorithm, the generalised conjugate gradient method, with a Block Incomplete Lower-Upper (BILU) factorization as a pre-conditioner.[24]

Several low-Mach number schemes have been implemented in HMB3 to limit the loss of accuracy and round-off errors caused by the great disparity between convective and acoustic wave speeds in low-speed flows. In this work, in particular, the standard Roe scheme modified with the explicit low-Mach method developed by Rieper[25] has been used.

Boundary conditions are set by using ghost cells on the exterior of the computational domain.

2.1. Actuator disk models based on circulation distribution

The implementation of the Actuator Disk concept requires the addition of source terms to the momentum and energy equations to impose the pressure Δp across the rotor disk surface F, depending on the rotor thrust coefficient C_T, and on the advance ratio μ. The flow field around the blades is not resolved and minimal computational cost is paid. If a uniform model is considered, the pressure jump can be written as

$$\Delta p = \frac{T}{F} = \mathrm{const}$$

or in non-dimensional form as:

$$\Delta\overline{p} = \frac{2\Delta p}{\rho V^2} \approx \frac{C_T}{\mu^2} \tag{1}$$

Hereρ is the air density, V is the rotor velocity with respect to the air, T is the rotor thrust, and μ is rotor advance ratio

$$\mu = \frac{V\cos\alpha_r}{V_{\mathrm{tip}}}$$

where $V_{\mathrm{tip}} = \Omega R$ is the blade tip speed,Ω is the rotor rotational speed, R is the radius, and α_r is the rotor disk plane tilt angle, positive for forward tilt (for $\alpha_r \approx 0^{\circ}$ it can be accepted $\cos\alpha_r \approx 1$).

In forward flight the rotor load distribution is not uniform, and an AD model should allow for the radial position$r$ on the blade, and the azimuth angle ψ to be accounted for. A widely accepted AD model, expresses the loading of a forward flying rotor with a distribution of the form

$$\Delta\overline{p} = \Delta\overline{p}_0 + \Delta\overline{p}_{1\mathrm{s}}\sin(r,\psi) + \Delta\overline{p}_{2\mathrm{s}}\cos(r,\psi)$$

where the coefficients $\Delta\overline{p}_0$, $\Delta\overline{p}_{1\mathrm{s}}$ and $\Delta\overline{p}_{2\mathrm{s}}$ depend on rotor radius and solidity, rotor attitude, advance ratio, thrust coefficient, lift coefficient slope and free stream velocity.

The AD models presented here are based on a surface circulation distribution in combination with empirical data or Blade Element Theory (BET) and Rotor Momentum Theory (RMT). For a single blade, the lift per unit radial distance can be written as[26,27]

$$\frac{\mathrm{d}T_\mathrm{B}}{\mathrm{d}r} = \rho U(r,\psi)\Gamma_\mathrm{B}(r,\psi) \tag{2}$$

or for an N-bladed rotor

$$\frac{\mathrm{d}T}{\mathrm{d}r} = N\frac{\mathrm{d}T_\mathrm{B}}{\mathrm{d}r} = \rho U(r,\psi)N\Gamma_\mathrm{B}(r,\psi) = \rho U(r,\psi)\Gamma(r,\psi) \tag{3}$$

where $\Gamma_\mathrm{B}(r,\psi)$ is the single blade circulation distribution, $\Gamma(r,\psi) = N\Gamma_\mathrm{B}(r,\psi)$ is the total rotor circulation, and $U(r,\psi) = \Omega r + \Omega R\mu\sin\psi$. Hence the local loading of the disk surface can be written as

$$\Delta p(r,\psi) = \frac{1}{2\pi r}\rho U(r,\psi)\Gamma(r,\psi) \tag{4}$$

or

$$\Delta p(r,\psi) = \frac{1}{2\pi r}\cdot\frac{\mathrm{d}T}{\mathrm{d}r}$$

The total thrust force averaged per a one blade revolution

$$T = \frac{1}{2\pi}\int_0^{2\pi}\mathrm{d}\psi\int_0^R\frac{\mathrm{d}T}{\mathrm{d}r}\mathrm{d}r$$

and this allows the rotor thrust coefficient to be estimated:

$$\begin{aligned} C_T &= \frac{1}{\Omega^2R^4\pi^2}\int_0^{2\pi}\mathrm{d}\psi\int_0^R U(r,\psi)\Gamma(r,\psi)\mathrm{d}r \\ &= \frac{2}{\rho\Omega^2R^4\pi}\int_0^{2\pi}\mathrm{d}\psi\int_0^R\Delta p(r,\psi)r\mathrm{d}r \end{aligned}$$

or

$$\begin{aligned} C_T &= \frac{1}{\Omega^2R^3\pi^2}\int_0^{2\pi}\mathrm{d}\psi\int_0^1 U(\bar{r},\psi)\Gamma(\bar{r},\psi)\mathrm{d}\bar{r} \\ &= \frac{2}{\pi\rho\Omega^2R^2}\int_0^{2\pi}\mathrm{d}\psi\int_0^1\Delta p(\bar{r},\psi)\bar{r}\mathrm{d}\bar{r} \end{aligned} \tag{5}$$

where $\bar{r} = \frac{r}{R}$ is the non-dimensional rotor radius. Using Eq. (4) one can also determine the averaged local disk loading as

$$\begin{aligned} \Delta p_\mathrm{a} &= \frac{\rho}{2\pi^2R}\int_0^{2\pi}\mathrm{d}\psi\int_0^1 U(\bar{r},\psi)\Gamma(\bar{r},\psi)\mathrm{d}\bar{r} \\ &= \frac{1}{\pi}\int_0^{2\pi}\mathrm{d}\psi\int_0^1\Delta p(\bar{r},\psi)\bar{r}\mathrm{d}\bar{r} \end{aligned} \tag{6}$$

or

$$\Delta\bar{p}_\mathrm{a} = \frac{1}{\pi}\int_0^{2\pi}\mathrm{d}\psi\int_0^1\Delta\bar{p}(\bar{r},\psi)\bar{r}\mathrm{d}\bar{r} = \frac{C_T}{\mu^2} \tag{7}$$

2.2. Simplified disk circulation distribution (Model AD1)

For a main rotor disk, the simplified circulation distribution can be accepted in the form[28]:

$$\Gamma(\psi) = \frac{\Gamma_0}{1+\frac{3}{2}\mu\sin\psi} \tag{8}$$

The average circulation distribution Γ_0 can be determined by

$$\Delta p_\mathrm{a} = \frac{T}{\pi R^2} = \frac{\rho}{2\pi^2R}\int_0^{2\pi}\mathrm{d}\psi\int_0^1 U(\bar{r},\psi)\Gamma(\psi)\mathrm{d}\bar{r} \tag{9}$$

Substitution of Eq. (8) into (9) and integration around the azimuth and along the rotor radius, results for Γ_0:

$$\Gamma_0 = \frac{3\pi C_T\Omega R^2\sqrt{4-9\mu^2}}{2\left(2\sqrt{4-9\mu^2}-1\right)}$$

2.3. Disk circulation distribution with BET (Model AD2)

Based on the BET, a circulation estimate is given in[28]:

$$\Gamma(r,\psi) = \frac{1}{2}NU(r,\psi)a_\infty c\alpha$$

where a_∞ is the lift curve slope of the aerofoil section, c is the blade chord, and α is the blade incidence angle

$$\alpha = \theta - \phi$$

Here ϕ is the angle between the resultant velocity and the blade reference plane and θ is the blade pitch angle

$$\theta = \theta_e(r) - \theta_1 sin\psi - \theta_2\cos\psi$$

where the angle $\theta_e(r)$ is due to the blade twist. For the present paper the linear blade twist is accepted: $\theta_e(r) = \theta_0 + \theta_{\mathrm{tw}}\frac{r}{R}$. The blade incidence maybe written as:

$$\alpha = \theta - \frac{U_P}{U_T}$$

The components U_P and U_T are

$$U_P = \Omega R(\lambda + \beta\mu\cos\psi) + \Omega r\frac{\mathrm{d}\beta}{\mathrm{d}\psi},\ U_T \approx U$$

The inflow factor λ is determined as

$$\lambda \approx \mu\alpha_r + \lambda_\mathrm{i}$$

to include the induction via λ_i as well as the disk tilt. The blade flap angle (between blade location and the reference plane) may be expressed as:

$$\beta = \beta_0 - \beta_1\sin\psi - \beta_2\cos\psi$$

Substitution to Eq. (5) allows for determination of the thrust coefficient of the rotor:

$$C_T = \frac{a_\infty\sigma}{2}\left[\left(\theta_0+\frac{\theta_\mathrm{tw}}{2}\right)\mu^2 - (\alpha_r+\theta_1)\mu + \frac{2\theta_0}{3} + \frac{\theta_{tw}}{2} - \lambda_\mathrm{i}\right] \tag{10}$$

where $\sigma = \frac{Nc}{\pi R}$ is the rotor solidity. For a case $\theta_\mathrm{tw} = \theta_1 = 0^\circ$ from Eq. (10) it follows:

$$C_T = \frac{a_\infty\sigma}{2}\left(\theta_0\mu^2 + \frac{2\theta_0}{3} - \mu\alpha_r - \lambda_\mathrm{i}\right)$$

which is similar to the formula, presented in the Ref. 29. For a first approximation it can be accepted that

$$\lambda_\mathrm{i} \approx \frac{1}{2}\sqrt{C_T}$$

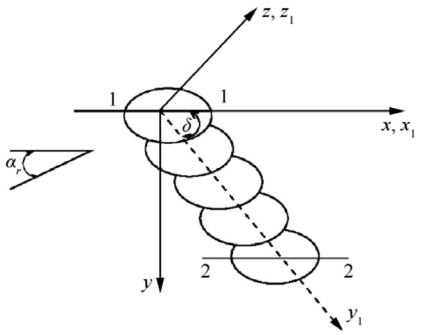

Fig. 1 Disk vortex set.[30]

2.4. AD theory, based on a "typical" circulation distribution and the vortex disk theory of main rotor (Model AD3)

Shaidakov's AD model[30] expresses the loading of a forward flying rotor with a non-uniform $\Delta p(r,\psi)$ distribution based on the combination of the surface disk circulation with RMT and BET.

The model accounts for blade tip offload, and for the rotor reversed flow region, as well as, for the blade root cutout. Its advantage is its efficiency and its ability to provide results with no iterative methods. Application examples of Shaidakov's model can be found in Ref. 31. The model originates from the theory of an ideal lifting rotor in incompressible flow and it has been tuned for realism using flight tests data. A brief description of the model in its first approximation is given below.

2.4.1. Vortex disk theory of main rotor with constant disk load

An ideal lifting system is considered as an arbitrary plate $F$with a constant disk load (Fig. 1).

The lifting system generates a set of closed vortex rings with an elementary vortex circulation$\mathrm{d}\Gamma_k$. For a linear approximation, the vortex rings are an inclined cylinder. Thus, one end part of cylinder (Section 1-1) is attached to the plane F, and the second end part (Section 2-2) is located at an infinite distance. The y axis of the Cartesian coordinate system is directed normally to the plate F, and the y_1 axis (of a skewed coordinate system) is directed along the cylinder axis. Circulation per length of the y_1 axis is determined as

$$\gamma = \frac{\mathrm{d}\Gamma_k}{\mathrm{d}y_1} = \mathrm{const}$$

Projections of the induced velocity vector on the y_1 axis at Sections 1-1 and 2-2 are determined as

$$v_{10} = \frac{\gamma}{2}, v_{20} = \gamma \tag{11}$$

and outside of the cylinder the following conditions are set:

$$v_{10} = v_{20} = 0$$

The vortex velocity V_{10} at the Section 1-1 in the direction of the y_1 axis can be determined as

$$V_{10} = v_{10}\mathrm{sign}\delta + V\cos(\alpha_r + \delta) \tag{12}$$

Here V is the free stream velocity, and $\delta$is the angle of vortex cylinder slope: $\delta > 0$ for the vortex set below the plate F.

According to Jukovsky's theorem[32] the normal (to F) elementary momentum contribution, per time$\mathrm{d}t$, for elementary circulation $\mathrm{d}\Gamma_k$, can be determined by:

$$\mathrm{d}M = \rho F \mathrm{d}\Gamma_k$$

Hence the thrust force is

$$T = \frac{\mathrm{d}M}{\mathrm{d}t} = \rho F \frac{\mathrm{d}\Gamma_k}{\mathrm{d}t} \tag{13}$$

The distance $\mathrm{d}y_1$which the vortex ring can pass at the Section 1-1 (see Fig. 1) can be determined as

$$\mathrm{d}t = \frac{\mathrm{d}y_1}{V_{10}} \tag{14}$$

Substituting Eqs. (10)–(12) and (14) to Eq. (13) yields:

$$T = \rho F \gamma V_{10} = \rho F v_{20}[v_{10}\mathrm{sign}\delta + V\cos(\alpha_r + \delta)] \tag{15}$$

One can note here that expressions (11) and (15) can be compared to similar expressions in Glauert's theory. The conditions (11) are similar to Glauert's conditions for the disk in-plane and far-field sections. However, in Shaidakov's theory the expressions (11) and (15) are written for the velocity vector along the y_1 axis, unlike Glauert's theory, where the similar conditions are formulated for the normal to the rotor disk v_{10n} and v_{20n} components (see, for example, Padfield[33]):

$$v_{10n} = v_{02n}, T = 2\rho F v_{10n} V_{10}$$

In a general case, when the load ("pressure jump" across the disk surface) Δp on the lifting system surface is not constant the plate F can be divided on a set of elementary plates $\mathrm{d}F$. In this case

$$\Delta p = \frac{\mathrm{d}T}{\mathrm{d}F}$$

and from (15) it follows that:

$$\Delta p = \rho\gamma V_{10} = \rho\gamma\left(\frac{\gamma}{2}\mathrm{sign}\delta + V\cos(\alpha_r + \delta)\right) \tag{16}$$

Solution the Eq. (16) for γ yields the expression

$$\gamma = \mathrm{sign}\delta\left[-V\cos(\alpha_r + \delta) + \sqrt{V^2\cos^2(\alpha_r + \delta) + \mathrm{sign}\delta\frac{2\Delta p}{\rho}}\right] \tag{17}$$

while the normalized aerodynamic load can be determined as

$$\Delta p = \frac{T}{\pi R^2} \tag{18}$$

Substituting Eq. (18) to Eq. (17) gives

$$\gamma = \mathrm{sign}\delta\left[-V\cos(\alpha_r + \delta) + \sqrt{V^2\cos^2(\alpha_r + \delta) + \mathrm{sign}\delta\frac{2T}{\rho\pi R^2}}\right]$$

or

$$\gamma = V\mathrm{sign}\delta\left[-\cos(\alpha_r + \delta) + \sqrt{\cos^2(\alpha_r + \delta) + \mathrm{sign}\delta\frac{2T}{\rho\pi R^2 V^2}}\right] \tag{19}$$

One can define the normalized free stream velocity$V$ and the circulation γ as:

$$V = \frac{V}{v_{1r}}, \gamma = \frac{\gamma}{v_{1r}}$$

where

$$v_{1r}^2 = \frac{T}{2\rho\pi R^2} = \frac{C_T}{\mu^2}\cdot\frac{V^2}{4} \tag{20}$$

Here $C_T = \frac{2T}{\rho\pi R^2\Omega^2R^2}$ is the thrust coefficient. One can note that for a cruise flight $\alpha_r + \delta \approx 0$. In this case Eq. (19) can be written as:

$$\tilde{\bar{\gamma}} = \tilde{\bar{V}}\,\mathrm{sign}\delta\left[-\cos(\alpha_r+\delta) + \sqrt{\cos^2(\alpha_r+\delta) + \mathrm{sign}\delta\frac{C_T}{\mu^2}}\right] \tag{21}$$

For a cruise flight $\frac{C_T}{\mu^2} \ll 1$, and hence

$$\tilde{\bar{\gamma}} = \tilde{\bar{V}}\,\mathrm{sign}\delta\left[-1 + \sqrt{1 + \mathrm{sign}\delta\frac{C_T}{\mu^2}}\right] \approx \tilde{\bar{V}}\frac{C_T}{2\mu^2} = \frac{2}{\tilde{\bar{V}}}$$

The angle of vortex cylinder slope approximately can be determined by the expression

$$\delta = \frac{\pi}{2} - \tan^{-1}\frac{\mu}{\lambda}$$

whereλ is the rotor inflow ratio.

2.4.2. Normalized aerodynamic loads for a typical disk circulation distribution

Expression (16) can be used for a more general case of a variable $\gamma(\bar{r},\psi)$ distribution:

$$\Delta p(\bar{r},\psi) = \rho\gamma(\bar{r},\psi)\left(\frac{\gamma(\bar{r},\psi)}{2}\mathrm{sign}\delta + V\cos(\alpha_r+\delta)\right) \tag{22}$$

The function $\gamma(\bar{r},\psi)$ is the distribution of circulation on the disk surface, and for a first approximation:

$$\gamma(\bar{r},\psi) = \gamma_r(\bar{r}) + \gamma_s(\bar{r})\sin\psi$$

where ψ is the azimuth angle of a considered point on the disk surface. The distribution of averaged blade load γ_r can be written as[26]:

$$\gamma_r(\bar{r}) = VAf_r(\bar{r}) \tag{23}$$

Here A is a constant, $f_r(\bar{r}) = \bar{r}^2(2-\bar{r}^2-\bar{r}^4)$. In Shaidakov's theory the expression for γ_r is determined for an admission thatΔp is a function of the disk radius only: $\Delta p(\bar{r},\psi) \approx \Delta p(\bar{r})$, (or $\frac{\partial\Delta p}{\partial r} \gg \frac{\partial\Delta p}{\partial\psi}$). Substituting Eq. (23) to Eq. (22) and non-dimensionalization leads to

$$\Delta\bar{p}(\bar{r}) = \frac{2\Delta p(\bar{r})}{\rho V^2} = A^2f_r^2(\bar{r}) + 2Af_r(\bar{r})\cos(\alpha_r+\delta) \tag{24}$$

The expression for constant A can be found from the integral condition (7):

$$\frac{1}{\pi}\int_0^{2\pi}\mathrm{d}\psi\int_0^1\Delta\bar{p}(\bar{r})\bar{r}\mathrm{d}\bar{r} \approx \frac{C_T}{\mu^2}$$

or

$$2\int_0^1\Delta\bar{p}(\bar{r})\bar{r}\mathrm{d}\bar{r} \approx \frac{C_T}{\mu^2} \tag{25}$$

Substituting Eq. (24) to Eq. (25) and after transformations gives:

$$A = -\frac{175}{88}\cos(\alpha_r+\delta) + \frac{175}{88} \times\sqrt{\cos^2(\alpha_r+\delta) + \frac{12}{5}\cdot\frac{88}{175}\frac{C_T}{\mu^2}} \tag{26}$$

The expression for the function$\gamma_s(\bar{r})$, that determines the azimuthal load distribution, was taken to be of the form:

$$\gamma_s(\bar{r}) = VAB\mu_v f_r(\bar{r})\left(\bar{r}^{-1} - \frac{25}{13}\bar{r}\right) \tag{27}$$

where B is a constant, $\mu_v = \mu + v_{xa}/(\Omega R)$. Taking into account Eq. (21), the average induced velocity v_{xa} is estimated as follows:

$$v_{xa} = \frac{V}{4}\left[-\cos(\alpha_r+\delta) + \sqrt{\cos^2(\alpha_r+\delta) + \mathrm{sign}(\delta)\frac{C_T}{\mu^2}}\right]k_\delta$$

where $k_\delta = \tan\left(\frac{\pi}{4} - \frac{|\delta|}{2}\right)$. In Shaidakov's theory a B constant (in Eq.(27)) is determined using the rotor parameters:

$$B = \frac{8\mu_v(1+k_\delta^2) + a_\infty\sigma k_\delta}{(1+k_\delta^2)(4\mu_v + a_\infty\sigma k_\delta)}$$

Here a_∞ is the lift coefficient slope andσ is the rotor solidity.

2.5. AD theory, based on a "typical" circulation distribution and disk surface averaged loading (model AD4)

2.5.1. Hover mode

In hover, expression (2) for the lift of a single blade, per the unit radial distance can be written as

$$\frac{\mathrm{d}T_\mathrm{B}}{\mathrm{d}\bar{r}} = R\rho U_\mathrm{H}(\bar{r})\Gamma_\mathrm{B}(\bar{r})$$

and the lift per unit radial distance for the rotor as:

$$\frac{\mathrm{d}T}{\mathrm{d}\bar{r}} = N\frac{\mathrm{d}T_\mathrm{B}}{\mathrm{d}\bar{r}} = R\rho U_\mathrm{H}(\bar{r})\Gamma(\bar{r})$$

where $\Gamma(\bar{r}) = N\Gamma_\mathrm{B}(\bar{r})$, $U_\mathrm{H}(\bar{r}) = R\Omega\bar{r}$. Hence the local load of a disk element can be written as

$$\Delta p(\bar{r}) = \rho\frac{U_\mathrm{H}(\bar{r})}{2\pi R\bar{r}}\Gamma(\bar{r}) \tag{28}$$

The distributed disk load $\Delta p(r)$ must satisfy condition (6):

$$\Delta p_\mathrm{a} = \frac{1}{\pi}\int_0^{2\pi}\mathrm{d}\psi\int_0^1\Delta p(\bar{r})\bar{r}\mathrm{d}\bar{r} \tag{29}$$

or

$$\Delta p_\mathrm{a} = 2\int_0^1\Delta p(\bar{r})\bar{r}\mathrm{d}\bar{r} \tag{30}$$

In Heyson and Katzoff[26], the circularly symmetric non-uniform relative pressure distribution ("typical load") was presented in the form

$$\bar{\gamma}_r(\bar{r}) = \frac{\Delta p(\bar{r})}{\Delta p_\mathrm{a}} \tag{31}$$

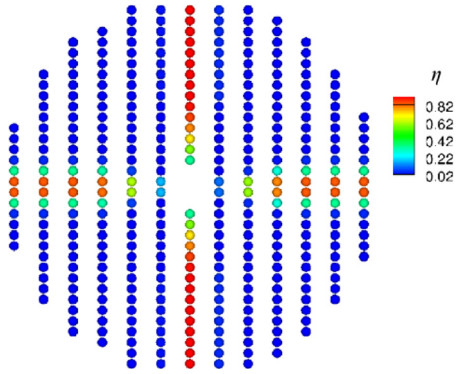

Fig. 2 Gaussian contribution function for VBA model.

From expressions (28) and (31) it follows that

$$\Gamma_r(\bar{r}) = \frac{\Delta p(\bar{r}) 2\pi R\bar{r}}{\rho U_{\mathrm{H}}(\bar{r})} = \Gamma_0 \bar{\gamma}_r(\bar{r}) \tag{32}$$

where

$$\Gamma_0 = \frac{2\pi \Delta p_{\mathrm{a}}}{\rho \Omega}$$

Using Eq. (32) expression (30) can be rewritten as

$$\Delta p_{\mathrm{a}} = 2\int_0^1 \frac{\rho \Gamma_0}{2\pi R} U_H(\bar{r}) \bar{\gamma}_r(\bar{r}) \mathrm{d}\bar{r}$$

Hence the function $\bar{\gamma}_r(\bar{r})$ must satisfy the condition:

$$2\int_0^1 \bar{\gamma}_r(\bar{r}) \bar{r} \mathrm{d}\bar{r} = 1 \tag{33}$$

The function $\bar{\gamma}_r(\bar{r})$ can be approximated by a polynomial

$$\bar{\gamma}_r(\bar{r}) = C\bar{r}^2\left(2 - \bar{r}^2 - \bar{r}^4\right) \tag{34}$$

and substituting Eq. (34) to Eq. (33) gives a constant C value:

$$C = \frac{12}{5} \tag{35}$$

2.5.2. *Forward flight mode*

In Heyson and Katzoff[26], it is noted that the pressure distribution $p(r)$ can be used for typical flight conditions including rotors in forward flight. For arbitrary flight conditions the non-uniform pressure distribution $\Delta p(r, \psi)$ is determined by expression (4). In the present work it is assumed that

$$\Gamma(\bar{r}, \psi) = \Gamma_r(\bar{r}) + \Gamma_s(\bar{r})\sin\psi = \Gamma_0(\bar{\gamma}_r(\bar{r}) + \bar{\gamma}_s(\bar{r})\sin\psi) \tag{36}$$

where

$$\Gamma_s(\bar{r}) = \Gamma_0 \bar{\gamma}_s(\bar{r})$$

Generalization of Eq. (31) yields

$$\Delta p(\bar{r}, \psi) = \Delta p_{\mathrm{a}} \bar{r}^{-1}(\bar{r} + \mu\sin\psi)[\bar{\gamma}_r(\bar{r}) + \bar{\gamma}_s(\bar{r}, \mu)\sin\psi] \tag{37}$$

It is evident that function $\bar{\gamma}_s(\bar{r}, \mu)$ should satisfy the condition

$$\bar{\gamma}_s(\bar{r}, 0) = 0 \tag{38}$$

In the present work, it is accepted that the function $\bar{\gamma}_s(\bar{r}, \mu)$ can be of the form:

$$\bar{\gamma}_s(\bar{r}, \mu) = K(\mu)\bar{\gamma}_r(\bar{r})\bar{r}^{-1}\left(1 - S(\mu)\bar{r}^2\right) \tag{39}$$

To determine $K(\mu)$ and $S(\mu)$ two conditions are necessary. The first condition is similar to expression (29), generalized for the non-uniform disk load distribution:

$$\Delta p_{\mathrm{a}} = \frac{1}{\pi}\int_0^{2\pi} \mathrm{d}\psi \int_0^1 \Delta p(\bar{r}, \psi)\bar{r}\mathrm{d}\bar{r} \tag{40}$$

The second is a trimming condition for the rolling moment:

$$M_x = R^3 \int_0^{2\pi} \mathrm{d}\psi \int_0^1 \Delta p(\bar{r}, \psi)\sin\psi \bar{r}^2 \mathrm{d}\bar{r} = 0 \tag{41}$$

Expressions (40) and (41) after substituting Eqs. (34) and (39) yield the system of equations

$$\left(-\frac{S(\mu)}{2} + \frac{7}{5}\right) = 0, \frac{K(\mu)}{2} + \frac{\mu}{2} - \frac{13K(\mu)S(\mu)}{50} = 0$$

Solution of this system gives for non-uniform pressure distribution:

$$S(\mu) = \frac{14}{5}, K(\mu) = \frac{125}{57}\mu \tag{42}$$

So, $\bar{\gamma}_r(\bar{r})$ and $\bar{\gamma}_s(\bar{r}, \mu)$ can be written as:

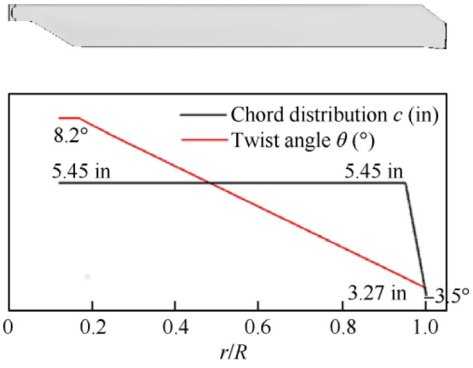

Fig. 3 Geometry of PSP model rotor with 60% taper and 30° swept tip.[36]

Table 1 Meshing parameters for PSP rotor mesh.

Mode	Fully resolved		AD mesh	
	Hover	FF	Hover	FF
Background mesh size (million of cells)	7.2	20	13.5	9
Blade mesh size (million of cells)	5.2	11.6	N/A	N/A
Overall mesh size (million of cells)	12.4 (1 blade)	31.6 (4 blades)	13.5 (4 blades)	9 (4 blades)
Points along span	215	145	N/A	N/A
Points around aerofoil	252	270	N/A	N/A

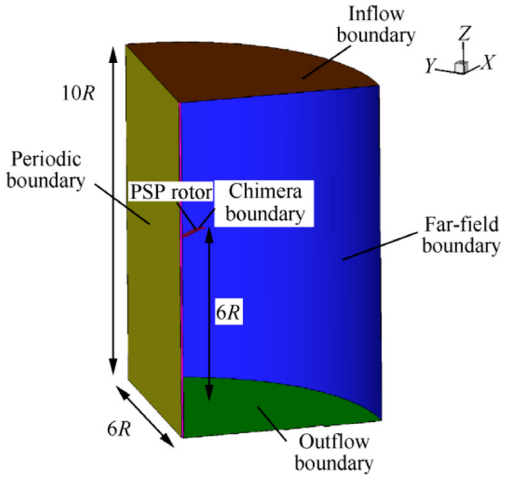

(a) Computational domain and boundary conditions

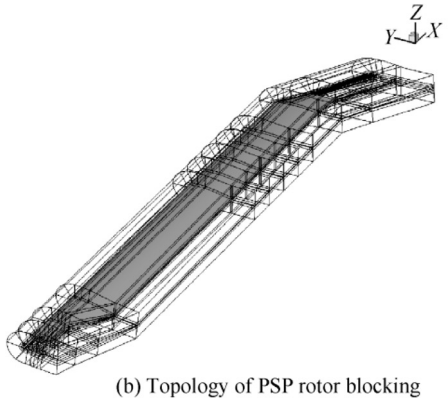

(b) Topology of PSP rotor blocking

Fig. 4 Computational domain and boundary conditions employed and topology of PSP rotor blocking.

$$\overline{\gamma}_r(\overline{r}) = \frac{12}{5}\overline{r}^2\left(2-\overline{r}^2-\overline{r}^4\right)$$
$$\overline{\gamma}_s(\overline{r},\mu) = \frac{125}{57}\mu\overline{\gamma}_r(\overline{r})\overline{r}^{-1}\left(1-\frac{14}{5}\overline{r}^2\right) \quad (43)$$

Expressions (37), (43) provide the disk load distribution. Expression (37) can be generalized to take into account a cosine cyclic component for the disk circulation distribution. To achieve this, Eq. (37) is rewritten in the following form:

$$\Delta p(r,\psi) = \frac{\Delta p_a}{\overline{r}}(\overline{r}+\mu\sin\psi)[\overline{\gamma}_r(\overline{r})+\overline{\gamma}_s(\overline{r},\mu)\sin\psi+\overline{\gamma}_c(\overline{r},\mu)\cos(2\psi)] \quad (44)$$

where $\overline{\gamma}_r(\overline{r})$ and $\overline{\gamma}_s(\overline{r},\mu)$ are determined by Eq. (43). For the function $\overline{\gamma}_c(\overline{r},\mu)$ the following structure is assumed:

$$\overline{\gamma}_c(\overline{r},\mu) = K(\mu)\overline{\gamma}_r(\overline{r})\left(1-W(\mu)\overline{r}^2\right) \quad (45)$$

Computations show, that to satisfy condition (41) ($M_x = 0$) the function $W(\mu)$ should be:

$$W(\mu) = \frac{25}{13}$$

Then, the condition for the pitching moment

$$M_z = -R^3\int_0^{2\pi} d\psi \int_0^1 \Delta p(\overline{r},\psi)\cos\psi\overline{r}^2 d\overline{r} = 0 \quad (46)$$

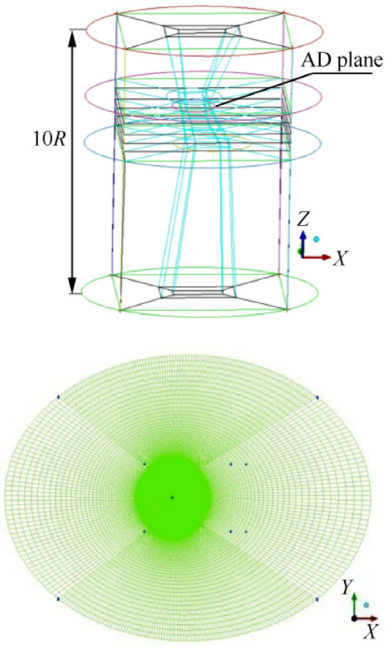

Fig. 5 Computational domain, multi-block topology and a section of CFD mesh for AD computations.

and Eq. (41) is satisfied automatically.

So, to determine the actuator disk load from Eq. (44) the functions $\overline{\gamma}_r(\overline{r})$, $\overline{\gamma}_s(\overline{r},\mu)$, and $\overline{\gamma}_c(\overline{r},\mu)$ can be written as:

$$\overline{\gamma}_r(\overline{r}) = C\overline{r}^2\left(2-\overline{r}^2-\overline{r}^4\right)$$

$$\overline{\gamma}_s(\overline{r},\mu) = K(\mu)\overline{\gamma}_r(\overline{r})\overline{r}^{-1}\left(1-S\overline{r}^2\right)$$

$$\overline{\gamma}_c(\overline{r},\mu) = K(\mu)\overline{\gamma}_r(\overline{r})\left(1-W\overline{r}^2\right)$$

where

$$C = \frac{12}{5}, K(\mu) = \frac{125}{57}\mu, W = \frac{25}{13}$$

Experimentation with symbolic algebra suggested that reducing the value of W to 16/13 and changing the functional form of $K(\mu)$ to be

$$K(\mu) = \frac{250\mu}{3(15\mu+38)} \quad (47)$$

resulted in better load distribution on the rotor disk, and again the M_x, and M_z moments were maintained to zero. This slightly better formulation was used for the results in this paper.

3. VBA model implementation

To introduce the effect of the rotating blades and to describe in more detail the rotor wake, the VBA model has been implemented in HMB3. For embedding of the AD models the local refinement of the grid cells using is accomplished using an additional grid splitting at a place of the disc localization. The virtual blades loading is distributed on the available grid cells. This allows for minimization of CPU time for determination of grid cells participating in a process of disk load distri-

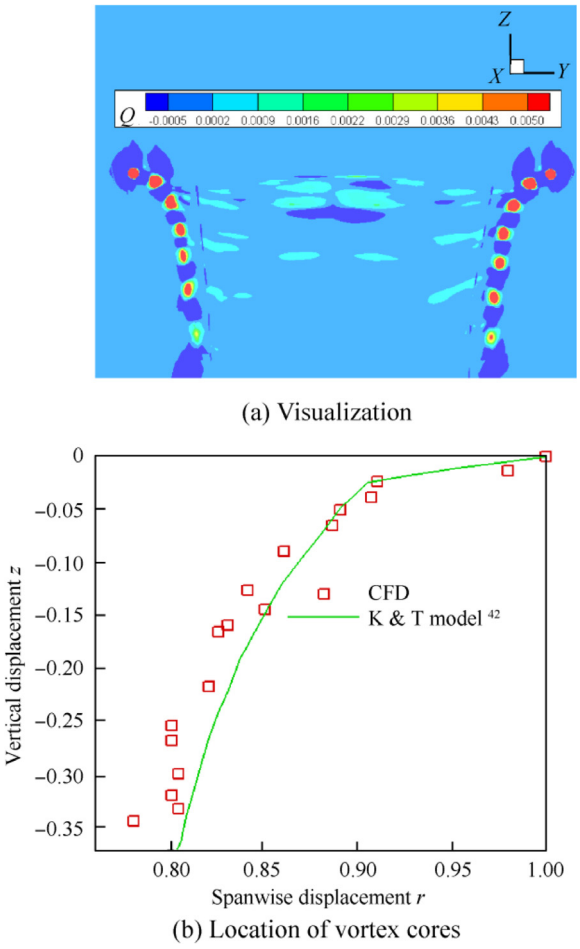

Fig. 6 Visualization of hovering rotor flow using with the $\overline{Q}$-criterion at symmetry plane section and location of vortex cores compared with the Kocurek & Tangler[42] model.

bution according to the virtual blade current azimuth. A Gaussian function $\eta$is used to shape the rotor load on the computational cells that belongs to the virtual blade. The source term $f(\bar{r},\psi)$ in the momentum equation in this case is therefore in the form

$$f(\bar{r},\psi)=\sum_{i=1}^{N_c}\frac{A_i\Delta p(\bar{r},\psi)}{|A|\sqrt{\pi}\sigma}\eta_i$$

where N_c is the number of cells belonging to the actuator disk, A_i the cell area and $\Delta p(\bar{r},\psi)$ is the pressure jump of the actuator disk from AD theory. The solidity σ of the virtual rotor is determined assuming that the planform of the blades is triangular until half of the rotor radius, to avoid root problems, and rectangular afterwards. The contribution of the Gaussian distribution η (see Fig. 2 as an example) of each blade to the considered CFD cell of the AD is defined as

$$\eta_i=\exp\left(-\frac{|s_i|^2}{\epsilon^2}\right)$$

where N is the number of blades, ϵ is the blade's mean aerodynamic chord and $|s_i|$ is the arc between the cell center and the actuator line.

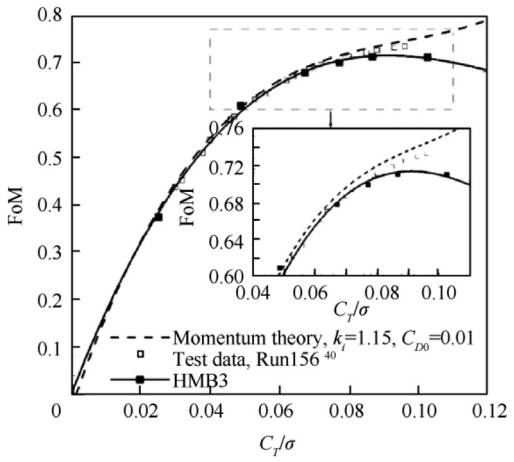

Fig. 7 FoM for PSP model rotor at blade-tip Mach number of 0.585.

Table 2 Computational cases for AD and CFD models.

Parameter	Low thrust	High thrust
C_T	0.008	0.016
Ma_{tip}	0.585	0.585
Ma_∞	0.2	0.2
α_r (°)	6.0	6.0
$\theta_{0.75}$ (°)	6.117	10.560
θ_{1s} (°)	4.536	8.956
θ_{1c} (°)	−2.558	−4.732
β_0 (°)	2.206	3.346
β_{1s} (°)	−0.501	−1.171
β_{1c} (°)	−0.252	−0.917

To guarantee that the total thrust is the same of the corresponding steady AD, the factor $|A|$ is used to normalise the source term at each time step:

$$|A|=\sum_{i=1}^{N_c}A_i$$

Thus, the cell distribution on the grid does not influence the global load of the rotor disk. Weighting in this way the effect of each point of the actuator disk, the presence of the blades is accounted for.

4. Numerical simulation of PSP rotor aerodynamics

To demonstrate the AD models presented in the previous paragraphs the isolated PSP model rotor blade is used with the HMB3 CFD solver[34] of Glasgow University.

4.1. PSP rotor geometry

The four-bladed PSP rotor has an aspect ratio (R/c) of 12.2 and a nominal twist of −14°. The main characteristics of the rotor blades are summarized in Table 1. The blade planform has been generated using three radial stations. First, the RC (4)-12 aerofoil was used up to 65%R. Then, the RC(4)-10 aerofoil from 70%R to 80%R. Finally, the RC(6)-08 aerofoil was

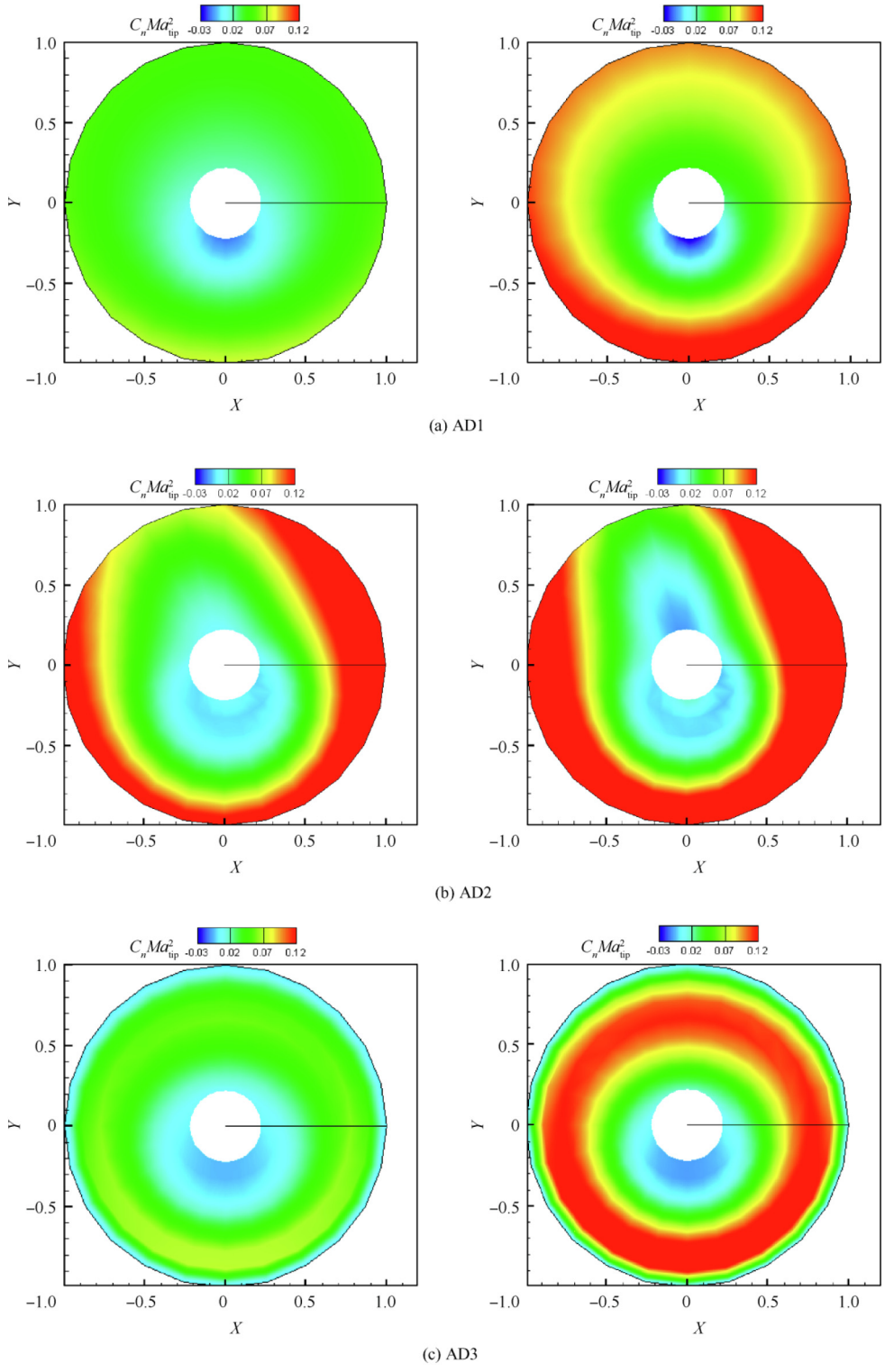

Fig. 8 Rotor disk air loads normal force Ma^2_{tip} coefficients in forward flight at advance ratio $\mu = 0.35$, $C_T = 0.008$ (left column), and $C_T = 0.016$ (right column) for different AD models and fully resolved blades.

used from 85%R to the tip. The aerodynamic characteristics of these aerofoils can be found in Refs. 35,36. The planform of the PSP model rotor has a 60% tapered and 30° swept tip and the details on the blade radial twist and the chord distributions are shown in Fig. 3.

4.2. PSP rotor mesh

For the blades, a C-topology around the leading edge of the blade was selected, whereas an H-topology was employed at the trailing edge.[37] For hover computations, only a quarter

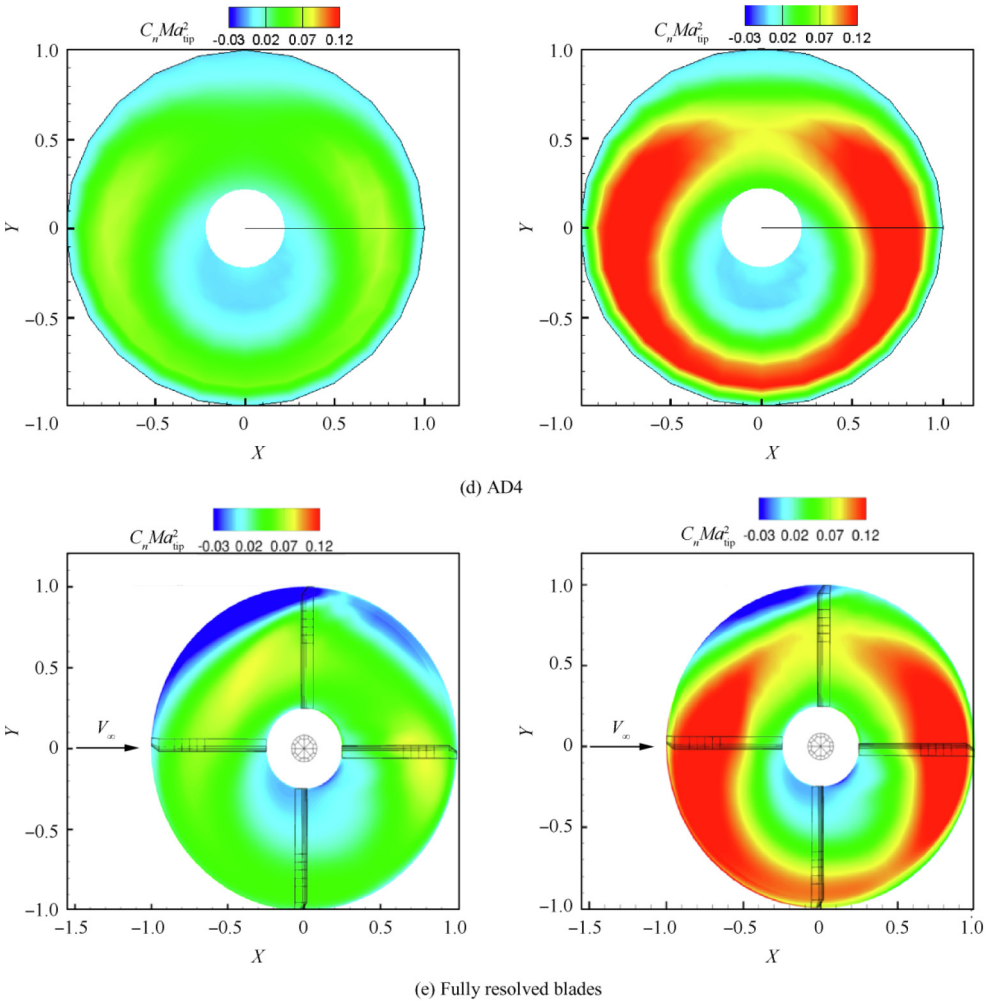

Fig. 8 (*continued*)

of the computational domain was meshed, assuming periodic conditions for the flow field in the azimuthal direction. This assumption is valid if the wake generated by the rotor is assumed periodic and the blades do not experience stall. The multi-block structured grid for the PSP rotor in forward flight has a total of 31.6 million cells with 1968 blocks, with 20 million and 11.6 million cells for the background and body-fitted grids, respectively. A hub is also included in the computational domain and modeled as a generic ellipsoidal surface. A view of the computational domain along with the employed boundary conditions for hover is given in Fig. 4.

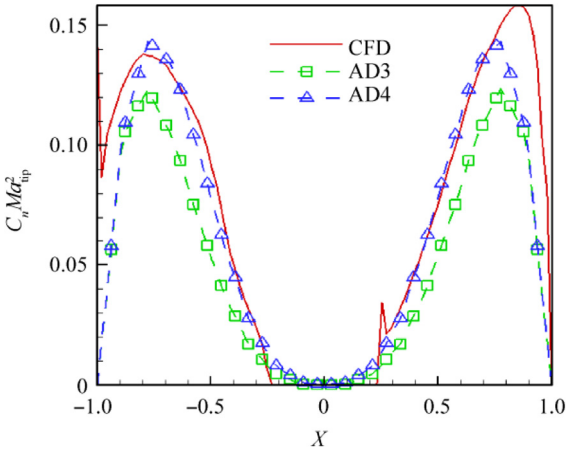

Fig. 9 AD3 and AD4 models compared to fully-resolved blades for the $C_nMa^2_{tip}$ coefficients in forward flight at advance ratio $\mu = 0.35$, $C_T = 0.016$.

The size of the employed computational domain and the multi-block mesh topology for AD simulations are presented in Fig. 5. The domain is similar in dimensions to what was used for the fully resolved rotor. The multi-block structured grid for the AD model in forward flight had a total of 9 million cells with 63 blocks and 13.5 million cells in hover. The multi-block structure in hover mode was adjusted for reproducing of the rotor tip vortex wake.

The meshing parameters for the PSP mesh rotor blade along with the grids used for hover and Forward Flight (FF) cases are shown in Table 1.

4.3. Test conditions and computations

In hover, the PSP blade was simulated at the blade-tip Mach number of 0.585. As a means to validate the PSP technique for rotor blades in hover, Wong et al.[38] and Watkins et al.[39]

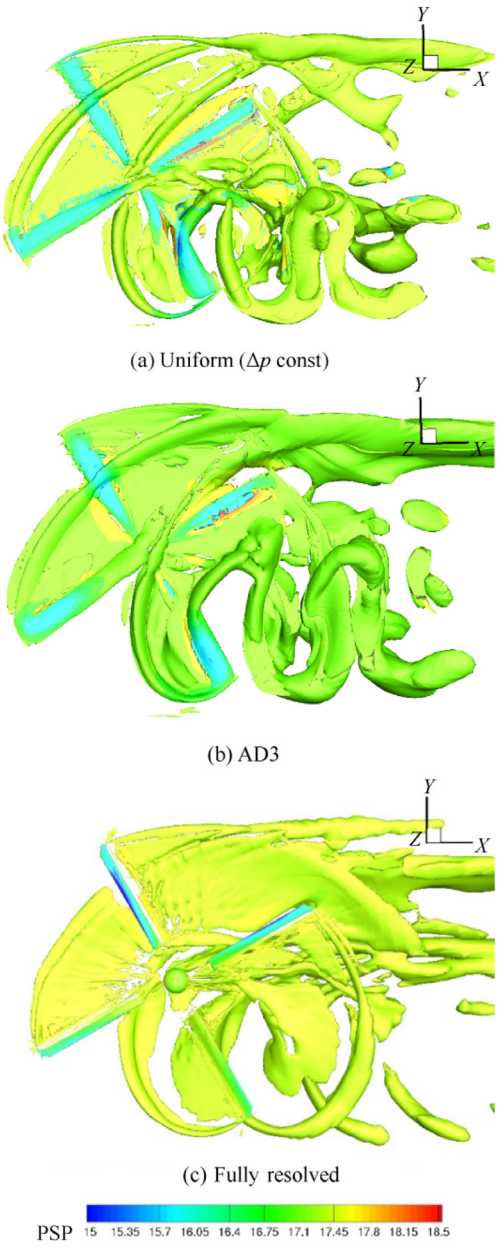

Fig. 10 Wake-visualisation of PSP rotor in forward flight at advance ratio $\mu = 0.35$ and $C_T = 0.008$ using $\overline{Q}$-criterion (value of 0.002) for different rotor blades models.

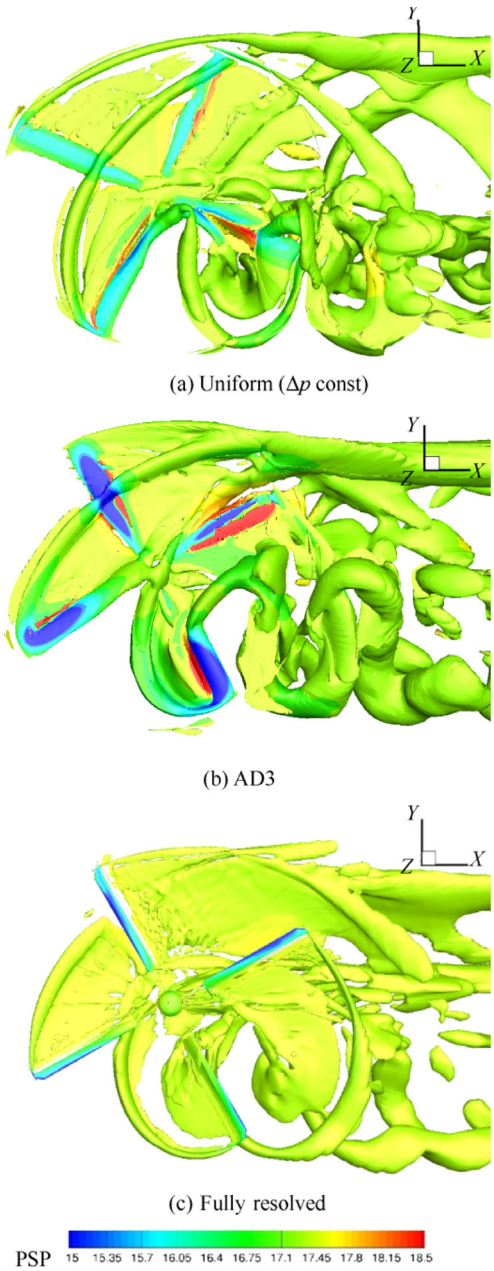

Fig. 11 Wake-visualisation of PSP rotor in forward flight at advance ratio $\mu = 0.35$ and $C_T = 0.016$ using $\overline{Q}$-criterion (value of 0.002) for different rotor blades models.

measured C_p at two radial stations at blade-tip Mach number of 0.585 on the PSP rotor blades, which were installed on the modified ROtor BOdy Interaction fuselage (ROBIN Mod7). Recently Overmeyer and Martin[40] extended this hover tests, measuring integrated blade loads for free and fixed transition and transition locations using the same conditions in the same facility (rotor test cell at the NASA Langley Research Center 14 ft × 22 ft Subsonic Wind Tunnel). This hover condition is simulated here in Out-of-Ground Effect (OGE) conditions for six blade pitch angles. Moreover, the effect of turbulence models on the integrated loads is also evaluated at fixed blade pitch angle ($\theta_{75} = 12°$). The Reynolds number, based on the reference blade chord c_{ref} of 5.45 inches and on the blade-tip speed, was 1.05×10^6.

Fig. 6 presents simulation results after 4 revolutions in hover for the AD3 model at blade-tip Mach number of 0.585, and $C_T = 0.016$. Fig. 6(a) shows visualization of the flow field using the $\overline{Q}$-criterion[41] at the symmetry plane. The location of the tip vortex cores at different flow sections is presented in Fig. 6(b) in comparison to the Kocurek and Tangler's[42] model. The comparison suggests that the Kocurek and Tangler's model agrees with simulation results especially for the early wake age.

The PSP main rotor was also simulated at forward flight.[34] Flight test data for forward flight was acquired by Wong et al.[43] at the 14 ft × 22 ft subsonic tunnel at the NASA Langley Research Center on the General Rotor Model System

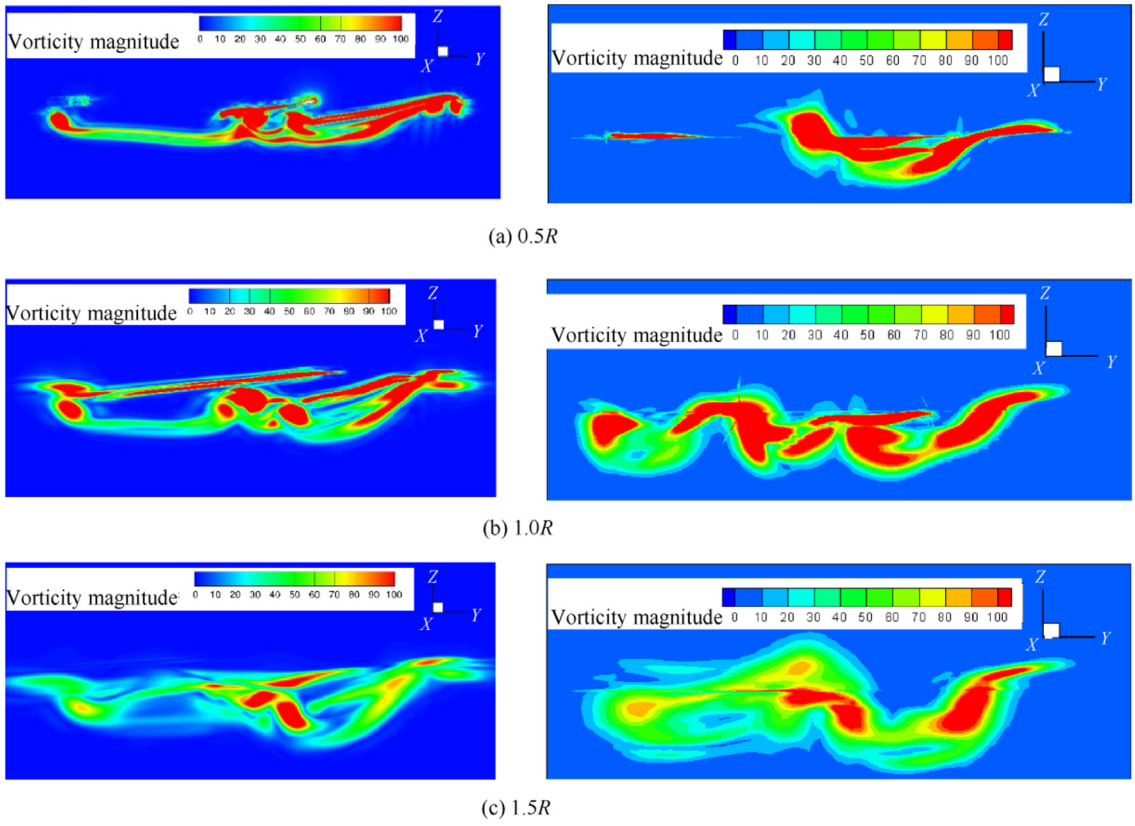

Fig. 12 Vorticity at 3 planes behind PSP rotor in forward flight at advance ratio $\mu = 0.35$ and $C_T = 0.008$ for the resolved (left column) and AD3 (right column) models.

(GRMS) test stand.[44] The rotor advance ratio was $\mu = 0.35$, and the free stream Mach number was 0.2. To meet the target thrust coefficient (blade loading coefficients C_T of 0.008 and 0.016) while having zero roll and pitch moments, a matrix trimming method is used in HMB,[14] based on the BET for computing the elements of the sensitivity matrix. The flow solutions were computed solving the URANS equations, coupled with Menter's[19] $k-\omega$ SST turbulence model. The employed time step corresponds to 0.25° in the azimuthal direction and was based on experience gained with previous rotor computations in forward flight.[45]

Fig. 7 shows the variation of Figure of Merit (FoM) vs the blade loading coefficient, at six blade pitch angles, covering low, medium, and high thrust. Comparison with experimental data (opened squares) by Overmeyer and Martin[40] for the fixed-transition, 5%c, upper and lower (Run 156) and momentum-based estimates of the FoM (dashed lines) are also included. For the momentum-theory estimation, and induced power factor k_i of 1.15 and overall profile drag coefficient C_{D0} of 0.01 were selected. The presented solutions agree very well with published solutions from several sources including Wong[46] who used the unstructured solver FUN3D and the Spalart-Allmaras[16] turbulence model, Vieira et al.[47] who employed commercial CFD, and Jain[48] who used the OVERFLOW solver. Note that the experiments reported here do not correspond to an isolated PSP rotor, and were obtained with a helicopter fuselage in place. Therefore some degree of discrepancy on the air loads is expected.

Ref. 49 shows in detail the numerical simulation results for the PSP and other rotors in hover and forward flight.

4.4. Comparison of simulation results for AD and resolved CFD models

The parameters of the AD pressure jump simulation for different AD models and for fully resolved blades simulation are presented in Table 2.

For the AD2 model a blade without twist was considered. Fig. 8 shows the normal force $C_n Ma_{\text{tip}}^2$ on the rotor disk of the PSP for different AD models in comparison to the CFD simulation result for fully-resolved blades. The Mach scaled normal force coefficient was estimated according to:

$$C_n Ma_{\text{tip}}^2 = \frac{2}{N\rho a^2 c}\cdot\frac{\mathrm{d}T}{\mathrm{d}r} = \frac{2\bar{r}\Delta\bar{p}(\bar{r},\psi)}{\sigma} C_T\left(Ma_{\text{tip}}\right)^2 \tag{48}$$

Abrupt reductions of these values in Fig. 8(e) (blue area) are found at the Advancing Blade Side (ABS) region ($90° < \psi < 180°$) due to high speed and low blade incidence. Fig. 8(d) corresponding to the AD4 model also reveals a small area of low normal force at the ABS region. However, the ABS region is still not matching the results with fully resolved blades.

Detailed comparison of the AD3 and AD4 models $C_n Ma_{\text{tip}}^2$ and CFD with resolved blades is presented in Fig. 9. As shown the AD4 model is a good approximation of the CFD simula-

tion results, with only slight under-prediction of the loads near the tip of the blade.

One can propose that the under-predicted loads near the blade tip follow from the accepted in the present work expression (23) for the $\gamma_r(\bar{r})$ distribution.[26] To improve the AD method accuracy one can correct the $\gamma_r(\bar{r})$ polynomial based on experimental and CFD investigations results.

Visualization of the flow fields of the PSP rotor with fully resolved and virtual blades using the $\overline{Q}$-criterion is presented in Figs. 10 and 11. Indicative results are shown here for two VBA models, including the uniform pressure jump distribution and the AD3 model. In the present research the area of the virtual blades corresponds to the planform area of the resolved blades.

The CFD results for both AD models capture well the main flow structures near and far of the rotor disk compared to the fully resolved blades case. One can note a different near-field vortex shape for the uniform and non-uniform VBA models. This is due to the more loaded (virtual) blade tip part and underloaded middle part. The tip vortex core size for the uniform AD load is also predicted slightly smaller than for the non-uniform AD3 model.

To further show the differences and similarities between the employed models, the vorticity field is used. Fig. 12 shows (for low thrust case) comparisons between the resolved blades and the unsteady AD for 3 planes at $0.5R$, $1.0R$ and $1.5R$. Although the results do not fully agree (as expected due to the differences in the fidelity of the methods) a similar range of values is seen for vorticity, several of the vortical structures are at similar locations. The lack of any thickness of the AD, and the lack of the exact loading and planform of the blade are the main reasons behind any differences. Nevertheless, at $1.0R$ behind the rotor, the wakes are not too dissimilar in overall structure and magnitude and the results of the AD method can be seen as a first approximation to a complex flow field.

Much the same way, comparisons for the high thrust case of the PSP blade can be seen in Fig. 13. Again vorticity is used and the resolved blades are compared with the unsteady AD model. The main differences are concentrated on the extend of the vortical structures. So close to the rotor, the wake is not yet configured as a disk with two tip vortices. The distribution of the blade load using the Gaussian law and the assumed blade shape of the AD method obviously play a key role. Nevertheless, given the efficiency of the method this is something to be tolerated. The AD even in unsteady mode requires fewer grid points and for the PSP computations savings in CPU time approach 100%. For the considered AD mesh taking a revolution with 360 iterations 72 h are consumed by using 24 processors compared to 192 h by 72 processors for the fully resolved blades rotor. Clearly the AD method is an approximation but it can provide interesting results for first approximations to flows with rotor wakes.

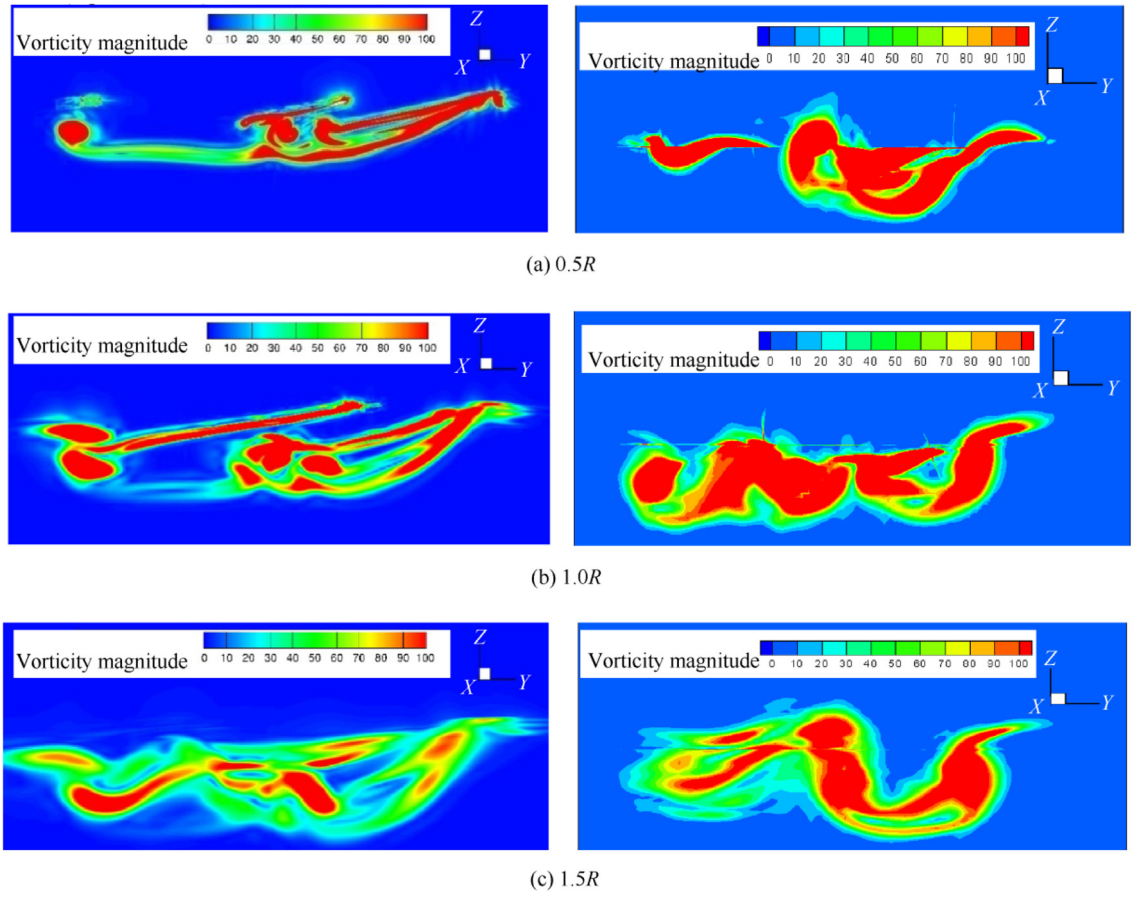

(a) $0.5R$

(b) $1.0R$

(c) $1.5R$

Fig. 13 Vorticity at 3 planes behind PSP rotor in forward flight at advance ratio $\mu = 0.35$ and $C_T = 0.016$ for the resolved (left column) and AD3 (right column) models.

5. Conclusions

The AD approach was applied to flows around helicopter main rotors. Several actuator disk formulations were considered with uniform and non-uniform disk loadings. The non-uniform ADs were based on prescribed disk circulation distributions (including blade element theory). Simulations with fully resolved blades were compared to unsteady AD implementations, to allow resolution of the unsteady rotor wake. Despite the reduced grid cells number, the CFD results for AD models captured well the main vortical structures around the rotor disk in comparison to the fully resolved cases. These AD models can be used for studies of the flow wake or for simple studies of rotor installation effects. Efforts to deliver trimmed ADs suitable for dynamic computations are currently underway.

Acknowledgements

This study was co-supported by the grant "State task of the Education and Science Ministry of Russian Federation" agreement (No. 075-03-2020-051/3 from 09.06.2020, theme No. fzsu-2020-0021).

References

1. Hansen MOL, Sørensen JN, Voutsinas S, et al. State of the art in wind turbine aerodynamics and aeroelasticity. *Prog Aerospace Sci* 2006;**4**:285–330.
2. Lynch CE, Prosser DT, Smith MJ. An efficient actuating blade model for unsteady rotating system wake. *Comput Fluids* 2014;**92**:138–50.
3. Sorensen JN, Shen WZ. Numerical modeling of wind turbine wakes. *J Fluids Eng* 2002;**124**:393–9.
4. Churchfield MJ, Schreck SJ, Martinez LA, et al. An advanced actuator line method for wind energy applications and beyond. *Proceedings of the 35th wind energy symposium*, 2017.
5. Modha AN, Blaylock TA, Chan WYF. Brown-out – flow visualisation using FLUENT VBM. *Proceedings of the international aerospace CFD conference*, 2007.
6. Renaud T, O'Brien D, Smith M, et al. Evaluation of isolated fuselage and rotor-fuselage interaction using CFD. *Proceedings of the American Helicopter Society 60th annual forum*, 2004.
7. O'Brien D, Smith M. Analysis of rotor-fuselage interactions using various rotor models. *Proceedings of the AIAA 43nd aerospace sciences meeting*, 2005.
8. Wang Q, Jiang Z, Zhang Q. Regionalized actuator disk model designed by optimization method for propeller slipstream computation. *Eng Appl Comput Fluid Mech* 2014;**8**(1):127–39.
9. O'Brien D. Analysis of computational modeling techniques for complete rotorcraft configurations dissertation. Georgia: Georgia Institute of Technology; 2006.
10. Kusyumov A, Mikhailov S, Phayzullin K, et al. Main rotor-body action for virtual blades model. EPJ Web Conf. 2017.
11. Li P, Zhao Q, Zhu Q. CFD calculations on the unsteady aerodynamic characteristics of a tilt-rotor in a conversion mode. *Chin J Aeronaut* 2015;**28**(6):1593–605.
12. Shen WZ, Zhang JH, Sorensen JN. The actuator surface model: a new Navier-Stokes based model for rotor computations. *J Sol Energy Eng* 2009;**131**(1) 011002.
13. Leishman JG. Principles of helicopter aerodynamics. 2nd ed. Cambridge: Cambridge University Press; 2006. p. 74–7.
14. Steijl R, Barakos G, Badcock K. A framework for CFD analysis of helicopter rotors in hover and forward flight. *Int J Numer Meth Fluids* 2006;**51**(8):819–47.
15. Boussinesq J. *Théorie de l'ecoulement tourbillonant et tumultueux des liquides dans des lits rectilignes àgrande section*. Tome I-II. 1st ed. Paris: Gaulthier-Villars; 1897.
16. Spalart P, Allmaras SR. A one-equation turbulence model for aerodynamic flows. *La Recherche Aérospatiale* 1994;**1**:5–21.
17. Spalart P. Strategies for turbulence modelling and simulations. *Int J Heat Fluid Flow* 2000;**21**(3):252–63.
18. Wilcox DC. Multiscale model for turbulent flows. *AIAA J* 1988;**26**(11):1311–20.
19. Menter FR. Two-equation eddy-viscosity turbulence models for engineering applications. *AIAA J* 1994;**32**(8):1598–605.
20. Menter FR, Egorov Y. A scale-adaptive simulation model using two-equation models. Reston: AIAA; Report No.: AIAA-2005-1095.
21. Osher S, Chakravarthy S. Upwind schemes and boundary conditions with applications to Euler equations in general geometries. *J Comput Phys* 1983;**50**:447–81.
22. Van Leer B. Flux-vector splitting for the Euler equations. *Proceedings of the eighth international conference on numerical methods in fluid dynamics*, 1982.
23. Van Albada GD, Van Leer B, Roberts Jr WW. A comparative study of computational methods in cosmic gas dynamics. In: Hussiani M, Leer B, Rosendal J, editors. *Upwind and high-resolution schemes*. Heidelberg: Springer; 1997. p. 95–103.
24. Axelsson O. Iterative solution methods. New York: Cambridge University Press; 1994.
25. Rieper F. A low-mach number fix for roe's approximate Riemann solver. *J Comput Phys* 2011;**230**:5263–87.
26. Heyson H, Katzoff S. Induced velocities near a lifting rotor with nonuniform disk loading. Washington, D.C.: NASA; 1957. Report No.: NACA TR 1319.
27. Johnson W. Helicopter theory. Dover Publication; 1994. p. 1089.
28. Martynov AK. Main rotor theory. Moscow: Machines Building (Mashinostrojenie); 1973. p. 362 (in Russian).
29. Seddon J, Newman S. Basic helicopter aerodynamics. New York: John Wiley & Sons Ltd; 2011. p. 255.
30. Shaidakov VI. Proceedings of Moscow Aviation Institute; 1978: 381 pp. (in Russian).
31. Kusyumov AN, Mikhailov SA, Romanova EV, et al. Simulation of flow around isolated helicopter fuselage. EPJ Web Conf. 2013.
32. Antropov VF, Burakov GB, Dyachenko AC, et al. Experimental researches on helicopter aerodynamics. Moscow: Machines Building (Mashinostrojenie); 1980. p. 240.
33. Padfield GD. Helicopter flight dynamics: the theory and application of flying qualities and simulation modelling. 2nd ed. Oxford: Blackwell Publishing; 2007. p. 641.
34. Jimenez-Garcia A, Barakos GN. Numerical simulations on the PSP rotor using HMB3. *Proceedings of the AIAA science and technology forum and exposition (SciTech 2018)*. Reston: AIAA; 2018.
35. Noonan KW. Aerodynamic characteristics of two rotorcraft airfoils designed for application to the inboard region of a main rotor blade. Washington, D.C.: NASA; 1990. Report No.: NASA TP-3009.
36. Noonan KW. Aerodynamic characteristics of two rotorcraft airfoils designed for the tip region of a main rotor blade. Washington, D.C.: NASA; 1991. Report No.: NASA TM-4264.
37. Jimenez-Garcia A, Barakos GN. Accurate predictions of rotor hover performance at low and high disk loadings. *J Aircr* 2017;**1**(1):1–12.
38. Wong OD, Noonan KW, Watkins AN, et al. Non-intrusive measurements of a four-bladed rotor in hover – a first look. *Proceedings of the American Helicopter Society aeromechanics specialists*, 2010.

39. Watkins AN, Leighty BD, Lipford WE, et al. Measuring surface pressures on rotor blades using pressure-sensitive paint. *AIAA J* 2016;**54**(1):206–15.
40. Overmeyer AD, Martin PB. Measured boundary layer transition and rotor hover performance at model scale. *Proceedings of the 55th aerospace sciences meeting*. Reston: AIAA; 2017.
41. Jeong J, Hussain F. On the identification of a vortex. *J Fluid Mech* 1995;**1**:69–94.
42. Kocurek JD, Tangler JL. A Prescribed wake lifting surface hover performance analysis. *J Am Helicopter Soc* 1977;**22**(1):24–35.
43. Wong OD, Watkins AN, Goodman KZ, et al. Blade tip pressure measurements using pressure sensitive paint. Proceedings of the 68th American Helicopter Society. 2012.
44. Gentry GL, Quinto PF, Gatlin GM, et al. The Langley 14- by 22-foot subsonic tunnel. Description. Flow characteristics and guide for users. Washington, D.C.: NASA; 1990. Report No.: NASA TP-3008.
45. Steijl R, Barakos GN. Sliding mesh algorithm for CFD analysis of helicopter rotor-fuselage aerodynamics. *Int J Numer Meth Fluids* 2008;**58**(5):527–49.
46. Wong TC. Application of CREATETM-AV helios in an engineering environment: hover prediction assessment. *Proceedings of the 55th aerospace sciences meeting*. Reston: AIAA; 2012.
47. Vieira BAO, Kinzel MP, Maughmer MD. CFD hover predictions including boundary-layer transition. *Proceedings of the 55th aerospace sciences meeting*. Reston: AIAA; 2017.
48. Jain RCFD. performance and turbulence transition predictions on an installed model-scale rotor in hover. *Proceedings of the 55th aerospace sciences meeting*. Reston: AIAA; 2017.
49. Barakos GN, Fitzgibbon T, Woodgate MA, et al. Numerical simulations of various rotor designs in hover and forward flight. *Proceedings of the AIAA science and technology forum and exposition (SciTech 2019)*. Reston: AIAA; 2019.